

An *in silico* study of electrophysiological parameters that affect the spiral-wave frequency in mathematical models for cardiac tissue

Mahesh Kumar Mulimani,^{1,*} Soling Zimik,^{1,†} and Rahul Pandit^{1,‡}

¹*Centre for Condensed Matter Theory, Department of Physics,
Indian Institute of Science, Bangalore 560012, India.*

Spiral waves of excitation in cardiac tissue are associated with life-threatening cardiac arrhythmias. It is, therefore, important to study the electrophysiological factors that affect the dynamics of these spiral waves. By using an electrophysiologically detailed mathematical model of a myocyte (cardiac cell), we study the effects of cellular parameters, such as membrane-ion-channel conductances, on the properties of the action-potential (AP) of a myocyte. We then investigate how changes in these properties, specifically the upstroke velocity and the AP duration (APD), affect the frequency ω of a spiral wave in the mathematical model that we use for human-ventricular tissue. We find that an increase (decrease) in this upstroke-velocity or a decrease (increase) in the AP duration increases (decreases) ω . We also study how other intercellular factors, such as the fibroblast-myocyte coupling, diffusive coupling strength, and the effective number of neighboring myocytes, modulate ω . Finally, we demonstrate how a spiral wave can drift to a region with a high density of fibroblasts. Our results provide a natural explanation for the anchoring of spiral waves in highly fibrotic regions in fibrotic hearts.

PACS numbers: 87.19.Xx, 87.15.Aa

I. INTRODUCTION

Nonlinear waves in the form of rotating spirals are ubiquitous spatiotemporal patterns that occur in a variety of biological or physical systems; these include chemical-reaction waves in the Belousov-Zhabotansky system [1–5], oxidation waves of carbon monoxide on the surface of platinum [6–8], calcium-signalling waves in *Xenopus oocytes* [9], cyclic-AMP signalling waves in the aggregation process of *Dictyostelium discoideum* [10, 11], and, notably, action-potential (AP) waves that mediate muscle contraction in cardiac tissue. The organization of these AP waves in the form of spirals or scrolls in cardiac tissue is associated with abnormal and life-threatening heart rhythms known as arrhythmias. In particular, ventricular arrhythmias can lead to sudden cardiac death; therefore, it is important to understand the dynamics of such waves.

The rhythm of a normal heart is maintained by the trains of waves that are generated by its pacemaker, the sino-atrial node (SAN). This normal rhythm in a heart can be disturbed by the formation of a spiral wave, which can override the function of the SAN as the primary source of waves and entrain the heart to follow the spiral-rotation frequency. There are multiple mechanisms through which spiral waves can occur in cardiac tissue [12–18]. A single-spiral state is associated with ventricular tachycardia (VT), which leads to a fast heart rate. A multiple-spiral state is linked to ventricular fib-

illation (VF) that results in a chaotic heart rate [13–15, 19–22], and a quivering of the left ventricle, which renders it incapable of pumping oxygenated blood to the body; and, in the absence of medical intervention, this leads to death in a few minutes. It is crucial, therefore, to develop a detailed understanding of how spiral waves in cardiac tissue can get destabilized and form multiple spiral waves. Some studies have shown that heterogeneity-induced spatial gradients in the frequency ω of a spiral wave can lead to such an instability [23, 24] or to the drifting of this spiral wave [20, 25–27]. We build on the results of these studies to investigate which physiological factors affect ω and how they modulate it. In mammalian hearts, cardiac tissue is heterogeneous: there can be cellular heterogeneity, e.g., cardiac fibroblasts in addition to myocytes, or a spatial variation of electrophysiological properties, e.g., along the apico-basal direction in a heart, or between intermural layers [28] of the heart, or because of conduction inhomogeneities [29].

We investigate the effects of various intracellular (ion-channel conductances) and intercellular (gap-junctional factors) parameters on the spiral-wave frequency. At the single-cell level, we show how changes in ion-channel conductances modulate action-potential (AP) properties, such as its upstroke velocity $\frac{dV}{dt}_{max}$ and duration (APD). We then examine how these changes in AP properties affect the spiral-wave frequency ω at the tissue level. We find that an increase (decrease) in $\frac{dV}{dt}_{max}$ (APD) increases (decreases) ω . We then investigate the effects of intercellular coupling strength on ω by changing the coupling strength in the following two ways: (a) by modifying the diffusion constant D of the medium; (b) by interspersing inexcitable point obstacles in the medium, thereby reducing the effective number of neighboring myocytes. We find that ω is unaffected by a change in D , but, with point obstacles, ω decreases with an increase

* maheshk@iisc.ac.in ;

† solyzk@gmail.com ;

‡ rahul@iisc.ac.in;

also at Jawaharlal Nehru Centre For Advanced Scientific Research, Jakkur, Bangalore, India

in the density of these obstacles. We examine two models for fibrosis, which occurs in diseased hearts and is usually accompanied by a proliferation of fibroblasts [30–34]. These models allow us to study how various fibroblast parameters, e.g., the fibroblast-myocyte coupling and the AP of the coupled myocyte, affect ω and spiral-wave dynamics; the fibroblast parameters include its resting potential and the number of fibroblasts coupled to a myocyte. Moreover, we show that a spiral in a medium with a heterogeneous distribution of fibroblasts, drifts towards the region with a high density of fibroblasts.

The paper is organized as follows. The Materials and Methods Section II contains (a) the details of the myocyte and tissue models that we use in our simulations and (b) the numerical techniques we use to solve the governing equations. We then provide the findings of our study in the Section III on Results. Finally, in the Discussion Section IV, we discuss our results in the light of other past studies and mention some of the limitations in our study.

II. MATERIALS AND METHODS

For myocytes we use the TP06 human-ventricular-cell model [35], in which the transmembrane potential V_m of an isolated myocyte is governed by the following ordinary differential equation (ODE):

$$\begin{aligned} \frac{dV_m}{dt} &= -\frac{I_{ion}}{C_m}, \\ I_{ion} &= \sum_i I_i; \end{aligned} \quad (1)$$

I_{ion} is the sum of all the ion-channel currents with I_i the i^{th} ion-channel current, and C_m the normalized transmembrane capacitance. In Table II we list the currents in the TP06 model; their dependence on V_m is given, e.g., in Ref. [35].

The spatiotemporal evolution of V_m in mathematical models for cardiac tissue is governed by the following reaction-diffusion partial differential equation (PDE):

$$\frac{\partial V_m}{\partial t} = D \nabla^2 V - \frac{I_{ion}}{C_m}; \quad (2)$$

D is the diffusion coefficient; we restrict ourselves to a scalar D for simplicity; the TP06 case is described in detail in their dependence on V_m is given, e.g., in Refs. [35]. It is convenient to use the following non-dimensionalised ion-channel conductances and diffusion coefficients:

$$S_G = \frac{G}{G_c}; S_D = \frac{D}{D_0}, \quad (3)$$

where G stands for a typical conductance, G_c is the control value of the conductance, and the control diffusion constant $D_0 = 0.00154 \text{ cm}^2/\text{ms}$; for the conductances we consider, $G_c = 14.838, 0.0000398, 0.153 \text{ pA/pF}$ for G_{Na}, G_{CaL} , and G_{Kr} , respectively.

We use the following two models for the fibroblast cells:

| | |
|------------|---|
| I_{Na} | fast inward Na^+ current |
| I_{CaL} | L-type inward Ca^{++} current |
| I_{to} | Transient outward current |
| I_{Ks} | Slow delayed rectifier outward K^+ current |
| I_{Kr} | Rapid delayed rectifier outward K^+ current |
| I_{K1} | Inward rectifier outward K^+ current |
| I_{NaCa} | Na^+/Ca^{++} exchanger current |
| I_{NaK} | Na^+/K^+ pump current |
| I_{pCa} | plateau Ca^{++} current |
| I_{pK} | plateau K^+ current |
| I_{bNa} | background inward Na^+ current |
| I_{bCa} | background inward Ca^+ current |

TABLE I. **The various ionic currents in the TP06 model [35]; the symbols used for the currents follow Ref. [35].**

- **Model I:** We model the fibroblast cells as inexcitable obstacles and we replace the myocytes at random with these inexcitable obstacle throughout our simulation domain such that the percentage of sites with obstacles is p_o . The gap-junctional current between the myocyte and inexcitable obstacles in this model is zero (see Refs. [29, 36]).
- **Model II:** We model the fibroblasts in our study as an electrically passive cell, as in Ref. [37]. Each myocyte is coupled to N_f fibroblasts; and the myocyte and fibroblast transmembrane potentials V_m and V_f , respectively, obey the following coupled ODEs:

$$\begin{aligned} \frac{dV_m}{dt} &= -\left(\frac{I_{ion}}{C_m} + N_f \times \frac{I_{gap}}{C_m}\right); \\ \frac{dV_f}{dt} &= \frac{(I_{gap} - I_f)}{C_f}; \\ I_f &= G_f (V_f - E_f); \\ I_{gap} &= G_{gap} (V_m - V_f). \end{aligned} \quad (4)$$

C_f , E_f , and G_{gap} are the membrane capacitance of a fibroblast, the fibroblast resting potential, and the fibroblast-myocyte gap-junctional coupling, respectively. We use a *bilayer model* for fibroblast-myocyte couplings: fibroblasts, in the top layer, are coupled to myocytes in the bottom layer, as in Ref. [16], which contains a schematic diagram of this bilayer and the PDEs that describe the spatiotemporal evolution of waves of activation in this model; we do not include fibroblast-fibroblast couplings. Moreover, when we consider a heterogeneous distribution of fibroblasts in Sec. IIID, we remove randomly all the N_f fibroblasts at a site in the top layer, so that the percentage of sites at which we retain fibroblasts is p_f . To study gradients in the density of fibroblasts, we use a space-dependent density that varies linearly as we move

away from chosen central site:

$$p_f(r_i) = p_f(r_0) - \frac{[p_f(r_0) - p_f(r_{max})]}{[r_{max} - r_0]} \times r_i, \quad (5)$$

where r_i is the distance from the centre, r_0 is the position of the centre, and r_{max} is maximum radial distance from the centre.

We update the ODEs via the forward-Euler method for Eqs. 1 and 4. For our two-dimensional (2D) tissue simulations as in Eq. 2 we use a square domain with $N \times N$ grid points with $N = 512$, the forward-Euler scheme for time marching, and a central-difference scheme with a five-point stencil for the Laplacian, with the time and space steps $\Delta t = 0.02 \text{ ms}$ and $\Delta x = 0.025 \text{ cm}$, respectively. The control value of the diffusion coefficient $D = D_0$, in Eqs. 2, is $D_0 = 0.00154 \text{ cm}^2/\text{ms}$, which gives us a conduction velocity $CV \simeq 70 \text{ cm/s}$, as has been reported for human-ventricular-tissue models [35, 38].

- We calculate the frequency ω by recording the time-series of the transmembrane potential V_m at four representative positions in the simulation domain. From the principal peak in the Fourier transforms of these time series, we obtain ω (we take the average of the values at the four representative positions). [We show in Table S1 of the Supplemental Material [39] that this frequency is within error bars of the frequency ω_{tip} of rotation of the tip of the spiral wave.]
- For the radius of the tip trajectory of a rigidly rotating spiral waves, which is, on average, circular, we fit the average trajectory to a circle with radius r and center (x_c, y_c) , by using a nonlinear regression model, to obtain the mean radius and the mean values of the coordinates of the center of the circle; we also calculate the standard deviation of the fluctuations in r by using the mean position of the center (x_c, y_c) and the coordinates (x, y) of the points that lie on the unaveraged tip trajectory that we compute .
- We calculate CV by pacing the simulations domain at one end with a pacing cycle length of 1 Hz; we use 20 pulses. We record the time series of V_m at two designated grid points A and B , which are separated by a distance l_{AB} . These grid points are chosen such that the line between the two grid points is normal to the wavefront. We obtain the times t_A and t_B at which the wavefront hits the grid points A and B , respectively; the difference $t_B - t_A$ gives the time taken by the wavefront to propagate A to B ; therefore, $CV = \frac{l_{AB}}{(t_B - t_A)}$. In the disordered case, with inexcitable obstacles distributed at random in the simulation domain, we record the time series of V_m at multiple points and repeat the above procedure; we then take the mean of the CVs obtained from these points; we also compute the standard deviation of the CVs.

III. RESULTS

We present the results of our *in-silico* studies as follows: In Subsection III A we examine the dependence of the AP and of ω on various ion-channel conductances. Subsection III B is devoted to the effects of the gap-junctional coupling on ω . In Subsection III C we investigate the effects of the fibroblast-myocyte coupling on the myocyte AP and ω . We elucidate the drift of spiral waves in domains with an inhomogeneous distribution of fibroblasts in Subsection III D.

A. Effects of conductances on the AP and the spiral-wave frequency ω

The cell membrane of a myocyte is embedded with various ion-channels, which we list in Table II; V_m depends on the currents through these ion-channels (Eq. 1), so, if we vary the conductances of these channels, we can modulate the AP of the myocyte. To study the effects of these ion channels on the AP, we choose three representative major ionic currents for our study: I_{Na} , I_{CaL} , and I_{Kr} . Figure 1 (a) shows the APs of a myocyte for control values (magenta) and for the cases where the conductances G_{Na} (black), G_{CaL} (blue), and G_{Kr} (red) are increased three-fold. We find that increasing G_{CaL} (G_{Kr}) increases (decreases) the APD, whereas G_{Na} has no significant effect on the APD (Fig. 1 (b)). This is because the inward current I_{CaL} augments depolarization, and I_{Kr} , being an outward current, enhances repolarization; although I_{Na} is an inward current, it is active only during the early upstroke phase of the AP, therefore, it cannot affect the APD significantly. Furthermore, we find that increasing G_{Na} increases the upstroke velocity $\frac{dV}{dt}_{max}$, but G_{CaL} and G_{Kr} do not affect on $\frac{dV}{dt}_{max}$ (see Fig. 1). We have also checked the effects of other ion-channel conductances and ion-pump parameters on the AP. The results are consistent with our findings above, namely, increasing (decreasing) the conductances of inward (outward) currents increases (decreases) the APD of the myocyte; and I_{Na} is the only current that can change the value of $\frac{dV}{dt}_{max}$. We give details in Fig. S1 in the Supplemental Material [39].

We now study how these changes in $\frac{dV}{dt}_{max}$ and the APD affect the dynamics of a spiral wave. In Fig. 2 (a) we show spiral-tip trajectories and how the radius r , of the averaged circular trajectory, varies with the three conductances G_{CaL} (blue), G_{Na} (black), and G_{Kr} (red); the columns are labelled by the values of S_G (Eq. 3), which multiply only the conductance that labels a row (all other conductances are held at their control values as we move along a row in Fig. 2 (a)). In Figs. 2 (b), (c), and (d) we give plots versus S_G of, respectively, r , CV, and ω , for all these three conductances. In particular, we find that ω increases if we increase the values of G_{Na} and G_{Kr} ; by contrast, ω decreases as we increase G_{CaL} . This is consistent with the variation of r and of CV with S_G (Figs. 2 (b) and (c)), for ω is related to r and CV as

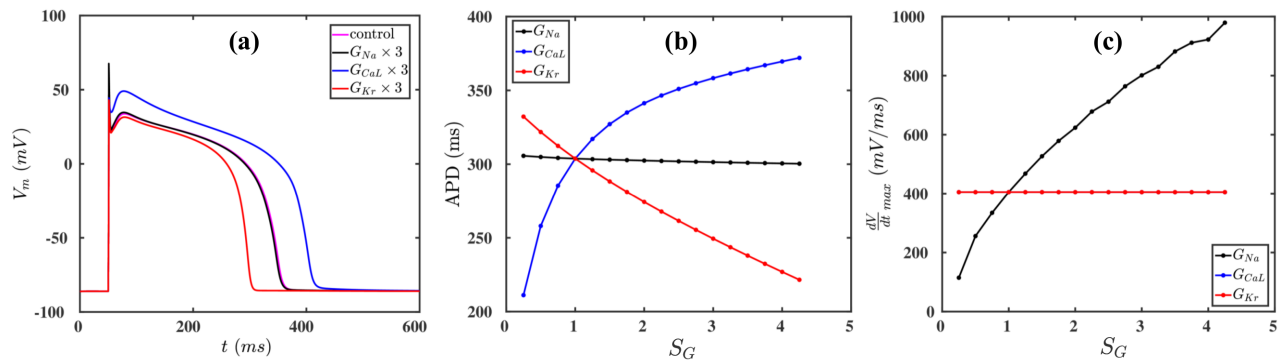


FIG. 1. (a) Action-potential plots for the control parameter set (magenta) and the cases when the conductances G_{Na} (black), G_{CaL} (blue), and G_{Kr} (red) are increased by a factor of three relative to their control values. (b) and (c): Plots of the APD and $\frac{dV}{dt}_{max}$, respectively, versus S_G , the non-dimensionalized conductance 3.

in Eq. 6. If we raise the values of G_{CaL} and G_{Kr} , then we find an increase and decrease the spiral core radius r , respectively, whereas G_{Na} has no significant effect on the value of r (Fig. 2 (b)). Furthermore, Fig. 2 (c) shows that CV increases with G_{Na} , whereas G_{CaL} and G_{Kr} do not affect CV; this is because only G_{Na} affects the value of $\frac{dV}{dt}_{max}$ (Fig. 1 (c)), which determines how fast a myocyte is excited and, therefore, how rapidly a wave of excitation propagates through our cardiac-tissue model. This result, along with Fig. 1 (b), implies that the change in the APD is associated with the change in the value of r ; a large (small) value of the APD is associated with a large (small) value of r ; and conductances such as G_{Na} have no significant effect on the APD because they do not affect r substantially. We have also checked this correlation between the APD and r for other conductances (see Fig. S2 in the Supplemental Material) and have found similar results. In summary, the rise of ω with the increase of G_{Na} is primarily because of the increase in CV, and the decline (rise) of ω , with the increase of G_{CaL} (G_{Kr}), can be attributed principally because to the increase (decrease) in r .

$$\omega \propto \frac{CV}{2\pi r} \quad (6)$$

B. Effect of the gap-junctional coupling on ω

The strength of the gap-junctional coupling between the cells in cardiac tissue can change in diseased conditions, e.g., in the wake of a myocardial infarction [40–42]. It is, therefore, instructive to investigate the role of the diffusive coupling between the cells on spiral-wave dynamics. To study the effect of D on ω , we first plot, in Fig. 3 (a), r (blue curve) and CV (red curve) versus S_D , the non-dimensionalised diffusion constant in Eq. 3; this shows that both r and CV increase with S_D , because a high diffusive coupling enhances the propagation of waves. The increase in CV is offset by the increase in

r , so ω (see Eq. 6) does not depend on S_D significantly, as we show in Fig. 3 (b).

We can also reduce the effective coupling strength between the cells in the medium by interspersing the medium with inexcitable point obstacles. These obstacles mimic collagen deposits in fibrotic tissue [30, 43]. The random distribution of these obstacles disrupts the propagation of a wave, as we show by the pseudocolor plots of V_m in Fig. 4 (a); and it reduces the velocity of the wave [29, 40]. In Fig. 4 (b) we plot CV versus p_o ; clearly, CV decreases as the obstacle density p_o increases; and beyond $p_o \simeq 38\%$, we observe *conduction block* with CV=0. This reduction in CV, with the increase of p_o , contributes to the decline of ω with increasing p_o , which we depict by the plot in Fig. 4 (c). Furthermore, because of the disorder-induced corrugated wavefront (Fig. 4 (a)), it becomes difficult to track the spiral-tip trajectory for $p_o > 10\%$; for $p_o < 10\%$, the value of r remains unaltered (see Fig. S3 in the Supplementary Material). Nonetheless, the simultaneous decrease of ω and CV, as we increase p_o , tells us that the change in CV is responsible principally for the variation of ω .

C. Effect of the fibroblast-myocyte coupling on AP properties and ω

Fibroblast cells, which maintain the structural integrity of a heart, are known to (a) proliferate in diseased conditions [30, 31] and (b) form gap-junctional couplings with myocytes. Such couplings can modulate the electrophysiological properties, e.g., of the AP, of the myocytes [37, 44, 45]. We show in Figs. 5 (a) and (b), how the fibroblast-myocyte coupling affects the AP morphology, APD, and $\frac{dV}{dt}_{max}$ for different values of fibroblast resting potential E_f and the number N_f of fibroblasts coupled to a myocyte in **Model II**. We see that the APD and $\frac{dV}{dt}_{max}$ increase and decrease, respectively, as we increase E_f . For a fixed value of E_f , increasing N_f decreases both APD and $\frac{dV}{dt}_{max}$. This is because fibroblasts act as

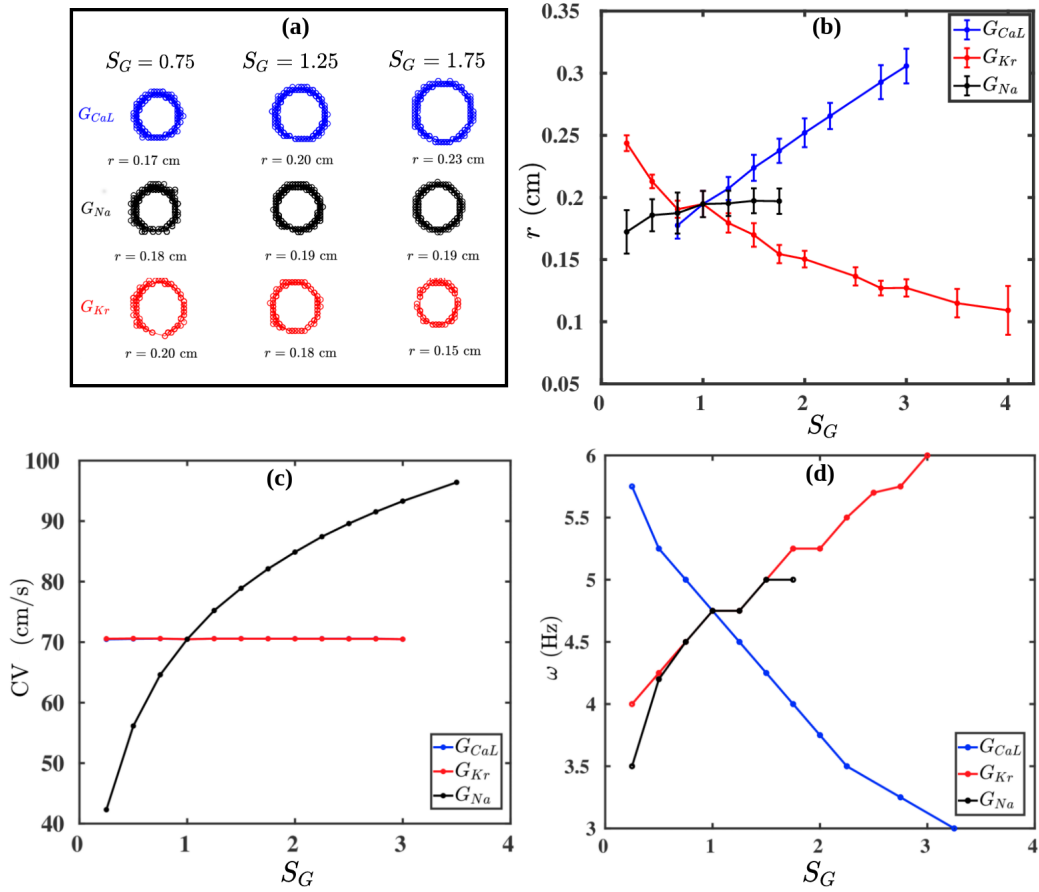


FIG. 2. (a) Traces of the tip trajectories of a spiral for different values of conductances of three ion-channels: G_{CaL} (blue), G_{Na} (black), and G_{Kr} (red); the columns indicate S_G (Eq. 3), which multiplies only the conductance that labels a row (all other conductances are held at their control values as we move along a row). (b), (c), and (d): Plots versus S_G of, respectively, r , CV, and ω (see text), for all these three conductances; one-standard-deviation error bars are shown for r .

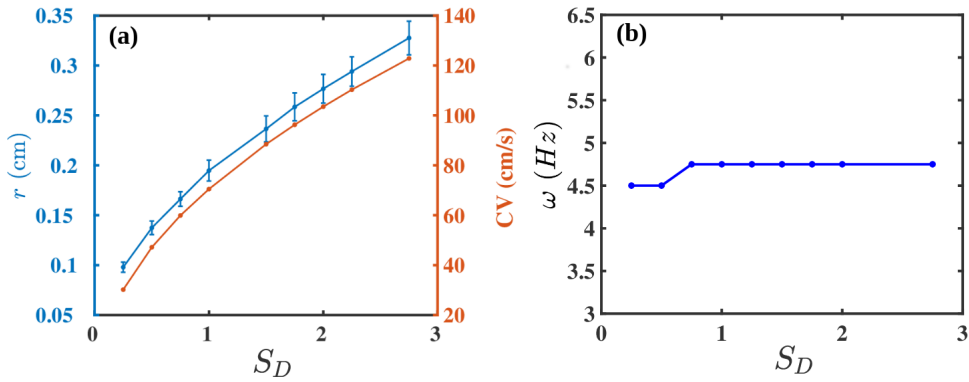


FIG. 3. Plots versus S_D (Eq. 3) of (a) r (blue curve) and CV (red curve) and (b) ω .

current sinks when coupled to myocytes. These changes in the properties of the AP, because of the fibroblast-myocyte coupling, affect the wave dynamics at the tissue level. We show in Fig. 5 (c) that the rise in the APD and the decline in $\frac{dV}{dt}_{max}$ (see Fig. 5 (b)) increases and decreases the values of r and CV, respectively, as we in-

crease E_f . In Fig. 5 (d) we show how the combination of these effects on CV and r affect the variation of ω with E_f and N_f .

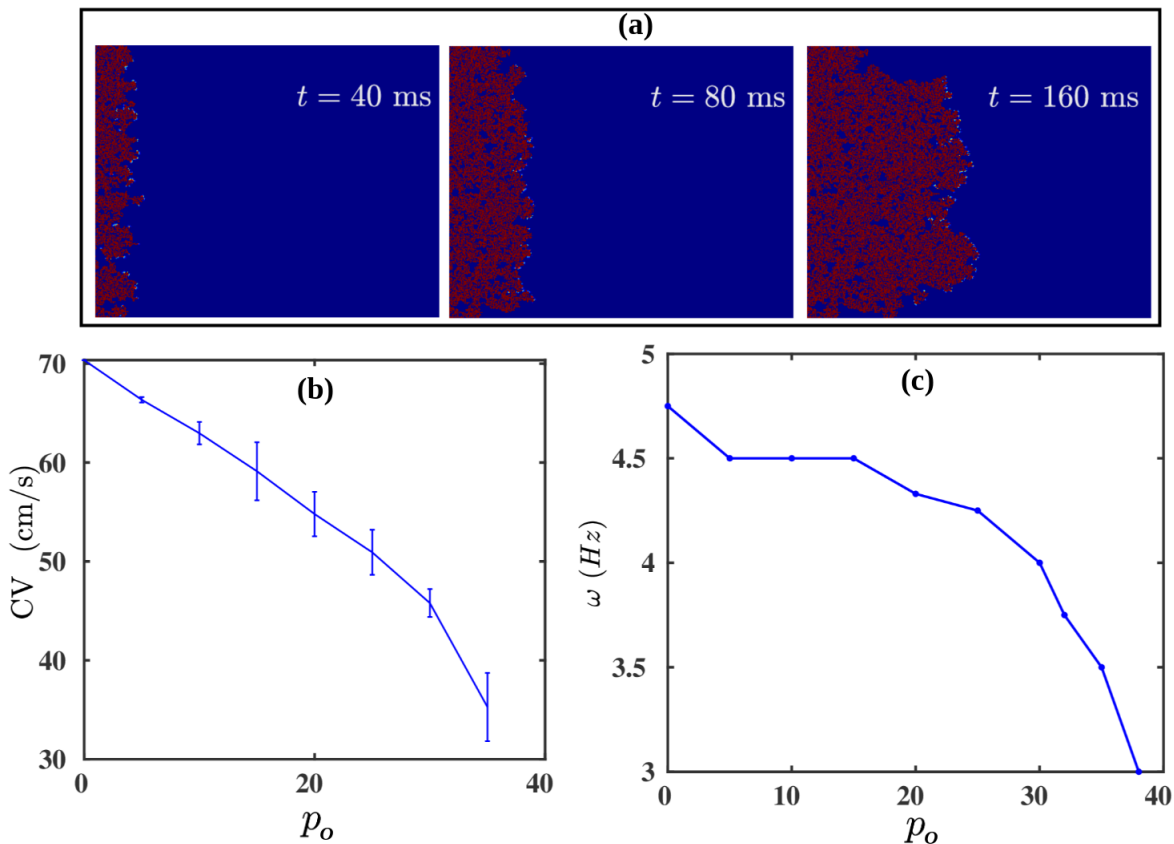


FIG. 4. (a) Pseudocolor plots of V_m illustrating the propagation of a plane wave through the simulation domain with randomly distributed inexcitable obstacles (**Model I**); the obstacle density $p_o = 35\%$. (b) and (c): Plots versus p_o of the plane-wave conduction velocity CV and the spiral-wave frequency ω . CV vanishes after $p_o \geq 38\%$; i.e., there is *conduction block*.

D. Drift of spiral waves in domains with an inhomogeneous distribution of fibroblasts

Fibrosis is a natural wound-healing process that occurs in the heart after a patient suffers from a condition such as infarction or heart attack [32–34], and such fibrotic tissue can affect the propagation of excitation waves [14, 29, 40, 41, 46, 47], which can promote arrhythmias. We now show how a heterogeneous density of fibroblasts in the medium can affect the dynamics of a spiral wave. Figure 6 (a) shows the heterogeneous distribution of fibroblasts in the medium; here, yellow indicates fibroblast-myocyte composites and blue indicates myocytes. The density of fibroblasts decreases radially outwards from the centre that is marked by a red octagram in Fig. 6 (a) (Sec. II Eq. 5). Figure 6 (b) shows the spatial variation of the APD in the medium because of the heterogeneous fibroblast density. Figures 6 (c) and (d) show the spatiotemporal evolution of a spiral in this case. It shows that a spiral, initiated at the left side of the domain in the region with a low density of fibroblasts, drifts towards the region with a high density of fibroblasts; and the spiral remains anchored to the central region, where the fibroblast density is maximum. The trajectory of the spiral tip is shown in white in Fig. 6

(d) (see also the video M1 in the Supplemental Material). This drifting of a spiral towards the region with a high density of fibroblasts is associated with the tendency of the spiral wave to drift towards a region high values of the APD [25, 26, 48–50]. Such anchoring of a spiral wave to a region with a high density of fibrosis has been seen in experiments on real hearts [19, 20, 51–53]. Our study illustrates how a region with a high density of fibroblasts can behave like an attractor and an anchoring point for spiral waves in fibrotic tissue. Such drifting of a spiral wave, in a medium with heterogeneity, has also been reported in other studies in contexts other than fibrosis [25, 26, 48–50].

IV. DISCUSSION

We have used *in silico* simulations of detailed mathematical models for cardiac tissue to examine the effects of various electrophysiological parameters of a cardiac cell and cardiac tissue on the AP properties and on electrical-wave dynamics. Our work is of relevance to such waves in real hearts, which are intrinsically heterogeneous along the transmural [28, 54, 55] and the apico-basal [56, 57] directions. Moreover, heterogeneities can be also be in-

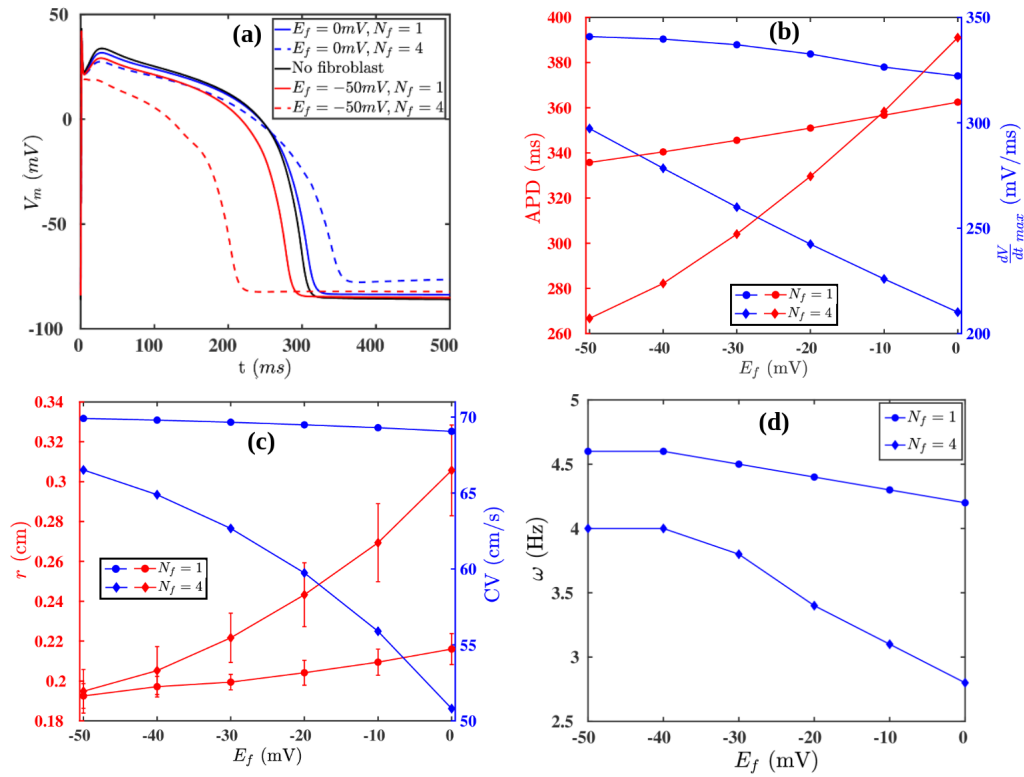


FIG. 5. (a) APs of an isolated myocyte (black -) and a myocyte coupled to fibroblasts with various parameters: $E_f = 0$ mV, $N_f = 1$ (blue -); $E_f = 0$ mV, $N_f = 4$ (blue -); $E_f = -50$ mV, $N_f = 1$ (red -); $E_f = -50$ mV, $N_f = 4$ (red -). (b) The values of the APD and $\frac{dV}{dt}_{max}$ for different values of E_f and two different values of N_f . (c) The values of r and CV for different values of E_f and two different values of N_f . (d) The variation of ω with changes in E_f for two different values of N_f .

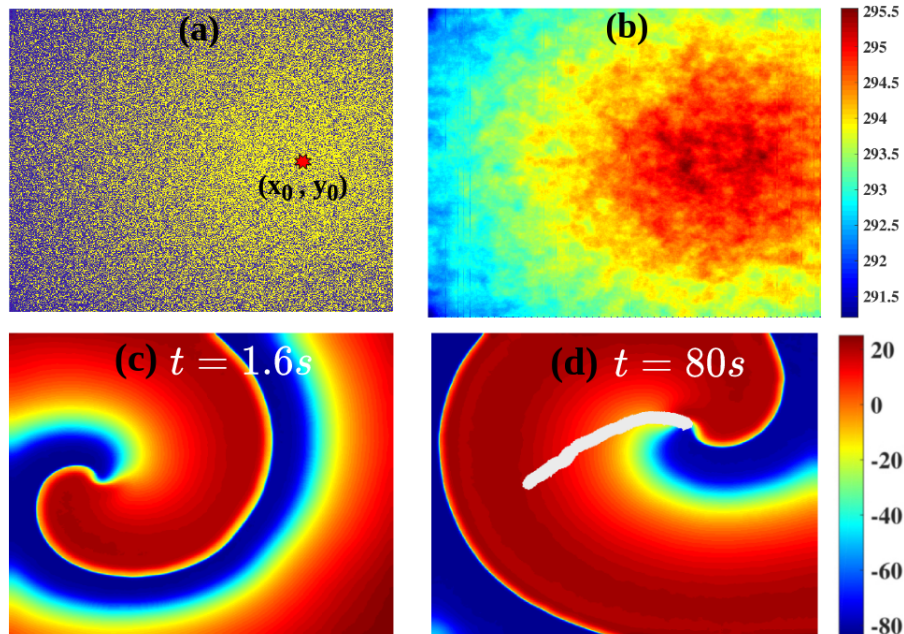


FIG. 6. (a) The radially decreasing distribution of the fibroblast density (**Model-II** Eq. 5) away from a center, marked by a red octagram; yellow indicates fibroblast-myocyte composites and blue denoted myocytes. (b) The distribution of the APD because of the gradient in fibroblast density. (c) and (d): pseudocolor plots of V_m showing a spiral wave in the simulation domain: a spiral initiated in the small-APD region, proximal to the left boundary, drifts towards the large-APD (low- ω) region. The tip trajectory of the spiral is marked by the white line.

duced in the heart because of diseases [56, 58–60]. In this context, we have shown how changes in various ion-channel conductances of a myocyte or the fibroblast-myocyte coupling can modulate the AP of a myocyte. We have then checked how these changes affect the spiral-wave frequency ω . We find that an increase (decrease) in $\frac{dV}{dt}_{max}$ or decrease (increase) in the APD increases (decreases) ω : large values of $\frac{dV}{dt}_{max}$ increase CV; and a low APD is associated with low values of the mean spiral-tip-trajectory radius r ; these are related to ω through Eq. 6. Our study has provided a natural understanding of how changes in the AP, at the single-myocyte level, can be related to changes in ω at the cardiac-tissue level. Moreover, we have investigated how changes in the gap-junctional coupling between the cells and S_D affect ω . We have also reduced the effective coupling between the cells by interspersing the medium with inexcitable obstacles; ω changes with the density of the obstacles. It is of interest to investigate such effects on ω , because they provide insights into spiral-wave dynamics in excitable media with heterogeneities [60]. We illustrate this in detail in Fig. 6 for a simulation domain with a heterogeneous distribution of fibroblast; here, we demonstrate the drift of a spiral wave towards the region with a high density of fibroblasts; such a drift has been seen in real hearts [19, 51–53].

We have explored the validity of the frequency relation 6 (Ref. [15]) for a wide range of electrophysiological parameters in the models that we use. We show in Fig.S7 in the Supplemental Material Ref. [39] that our measurements of ω and $\frac{CV}{r}$ are consistent with a linear relation (see the fit that is indicated by a black line); at very low values of CV, e.g., near conduction block in Model I which accounts for fibrosis-induced disorder, this linear relation breaks down. The randomness in these models introduces error in the determination of r of the spiral wave, especially for large randomness; e.g., as we increase p_f , we observe, in Fig.S6 (Supplemental Material [39]) that the tip trajectory of the spiral wave becomes very noisy. Note also that the CV of a plane wave is distinct from CV_{tip} the velocity of the tip of the spiral wave as it goes around its trajectory (on average a circle with radius r); clearly, $\omega_{tip} = CV_{tip}/(2\pi r)$ (see Table.S1 in the Supplemental Material [39]).

Some earlier studies have investigated the properties of

spiral waves in two-variable mathematical models for cardiac [61–67]. However, such studies have been conducted in the weak- or strong-excitability limits; real cardiac tissue exhibits various degrees of excitability depending on different electrophysiological parameters. Our study, which employs electrophysiologically detailed mathematical models for cardiac tissue, has allowed us to study spiral-wave dynamics with greater realism than is possible with two-variable models for cardiac tissue. The drifting of a spiral wave towards regions with a large APD has been reported in contexts other than fibrosis [25, 26, 48–50]. Moreover, anomalous drift of a spiral towards a region with a small APD, which has been observed in generic models [26], is not seen in our study; and it is yet to be reported in any in any of the electrophysiologically-detailed mathematical models for the cardiac tissue. It is also observed in the two-variable models that the radius of the spiral tip trajectory is very large, in the weakly excitable limit, compared to what is observed in the strongly excitable limit [64, 68]. In case of our realistic models, if we consider two parameters that control excitability, e.g., G_{Na} and D , then we observe that r does not increase with a decrease in the value of G_{Na} (see Fig. 2); but we observe an increase in r , as we increase the value of D (see Fig. S5 of the Supplemental Material [39]). Hence our systematic study, which uses a detailed human-ventricular-tissue mathematical model, provides an important point of reference for future *in silico* and experimental studies of such spiral waves in cardiac tissue.

We end our discussion with some limitations in our study. We have used a monodomain model for cardiac tissue. Bidomain models of cardiac tissue account for the extracellular matrix. However, monodomain models have been proved to be good approximations of cardiac tissue for wave propagation [69] for the types of excitations we consider. Furthermore, our tissue model does not incorporate the effects of mechanical deformations, stretch-activated channels, and stress-dependent diffusion tensors [70–72]. Such deformations can affect the dynamics of spiral waves [73] and the drift of spirals in a heterogeneous medium; we defer an investigation of the interplay between deformation and drift for future work.

REFERENCES

-
- [1] A. Zaikin and A. Zhabotinsky, *Nature* **225**, 535 (1970).
 - [2] A. T. Winfree, *Science* **175**, 634 (1972).
 - [3] R. J. Field et al., *Chaos in chemistry and biochemistry* (World Scientific, 1993).
 - [4] E. Ott, *Chaos in dynamical systems* (Cambridge university press, 2002).
 - [5] S. H. Strogatz, *Nonlinear dynamics and chaos with student solutions manual: With applications to physics, biology, chemistry, and engineering* (CRC press, 2018).
 - [6] M. Falcke, M. Bär, H. Engel, and M. Eiswirth, *The Journal of chemical physics* **97**, 4555 (1992).
 - [7] R. Imbihl and G. Ertl, *Chemical Reviews* **95**, 697 (1995).
 - [8] A. Pande and R. Pandit (1999).
 - [9] J. Lechleiter, S. Girard, E. Peralta, and D. Clapham, *Science* **252**, 123 (1991).
 - [10] J. J. Tyson and J. Murray, *Development* **106**, 421 (1989).

- [11] J. Rietdorf, F. Siegert, and C. J. Weijer, *Developmental biology* **177**, 427 (1996).
- [12] A. Panfilov and B. Vasiev, *Physica D: Nonlinear Phenomena* **49**, 107 (1991).
- [13] Z. Lim, B. Maskara, F. Aguel, R. Emokpae, and L. Tung, *Circulation* **114**, 2113 (2006).
- [14] Y. Xie, A. Garfinkel, P. Camelliti, P. Kohl, J. N. Weiss, and Z. Qu, *Heart Rhythm* **6**, 1641 (2009).
- [15] Z. Qu, G. Hu, A. Garfinkel, and J. N. Weiss, *Physics reports* **543**, 61 (2014).
- [16] A. R. Nayak, T. Shajahan, A. Panfilov, and R. Pandit, *PloS one* **8**, e72950 (2013).
- [17] A. R. Nayak and R. Pandit, *Physical Review E* **92**, 032720 (2015).
- [18] S. Zimik and R. Pandit, *Scientific Reports* **7**, 15350 (2017).
- [19] J. M. Davidenko, A. V. Pertsov, R. Salomonsz, W. Baxter, and J. Jalife, *Nature* **355**, 349 (1992).
- [20] K. Ten Tusscher and A. V. Panfilov, *American Journal of Physiology-Heart and Circulatory Physiology* **284**, H542 (2003).
- [21] R. Clayton, O. Bernus, E. Cherry, H. Dierckx, F. Fenton, L. Mirabella, A. Panfilov, F. Sachse, G. Seemann, and H. Zhang, *Progress in biophysics and molecular biology* **104**, 22 (2011).
- [22] S. Alonso, R. W. dos Santos, and M. Bär, *PloS one* **11**, e0166972 (2016).
- [23] S. Zimik and R. Pandit, *New Journal of Physics* **18**, 123014 (2016).
- [24] S. Zimik, R. Pandit, and R. Majumder, *PloS one* **15**, e0230214 (2020).
- [25] V. Krinsky, E. Hamm, and V. Voignier, *Physical review letters* **76**, 3854 (1996).
- [26] S. Sridhar, S. Sinha, and A. V. Panfilov, *Physical Review E* **82**, 051908 (2010).
- [27] V. N. Biktashev, I. V. Biktasheva, and N. A. Sarvazyan, *PLoS One* **6**, e24388 (2011).
- [28] R. Wolk, S. M. Cobbe, M. N. Hicks, and K. A. Kane, *Pharmacology & therapeutics* **84**, 207 (1999).
- [29] K. H. ten Tusscher and A. V. Panfilov, *Multiscale Modeling & Simulation* **3**, 265 (2005).
- [30] K. T. Weber, Y. Sun, S. C. Tyagi, and J. P. Cleutjens, *Journal of molecular and cellular cardiology* **26**, 279 (1994).
- [31] I. Manabe, T. Shindo, and R. Nagai, *Circulation research* **91**, 1103 (2002).
- [32] G. C. Gurtner, S. Werner, Y. Barrandon, and M. T. Longaker, *Nature* **453**, 314 (2008).
- [33] A. Biernacka and N. G. Frangogiannis, *Aging and disease* **2**, 158 (2011).
- [34] S. Hinderer and K. Schenke-Layland, *Advanced drug delivery reviews* **146**, 77 (2019).
- [35] K. H. Ten Tusscher and A. V. Panfilov, *American Journal of Physiology-Heart and Circulatory Physiology* **291**, H1088 (2006).
- [36] R. Majumder, A. R. Nayak, and R. Pandit, *PLoS one* **7**, e45040 (2012).
- [37] K. A. MacCannell, H. Bazzazi, L. Chilton, Y. Shibukawa, R. B. Clark, and W. R. Giles, *Biophysical journal* **92**, 4121 (2007).
- [38] K. Ten Tusscher, D. Noble, P.-J. Noble, and A. V. Panfilov, *American Journal of Physiology-Heart and Circulatory Physiology* **286**, H1573 (2004).
- [39] Supplemental Material.
- [40] J. De Bakker, F. Van Capelle, M. J. Janse, S. Tasseron, J. T. Vermeulen, N. de Jonge, and J. R. Lahpor, *Circulation* **88**, 915 (1993).
- [41] J. H. King, C. L. Huang, and J. A. Fraser, *Frontiers in physiology* **4**, 154 (2013).
- [42] K. S. McDowell, H. J. Arevalo, M. M. Maleckar, and N. A. Trayanova, *Biophysical journal* **101**, 1307 (2011).
- [43] M. S. Spach and J. P. Boineau, *Pacing and clinical electrophysiology* **20**, 397 (1997).
- [44] V. Jacquemet and C. S. Henriquez, *Europace* **9**, vi29 (2007).
- [45] S. Zlochiver, V. Munoz, K. L. Vikstrom, S. M. Taffet, O. Berenfeld, and J. Jalife, *Biophysical journal* **95**, 4469 (2008).
- [46] T. Kawara, R. Derksen, J. R. de Groot, R. Coronel, S. Tasseron, A. C. Linnenbank, R. N. Hauer, H. Kirkels, M. J. Janse, and J. M. de Bakker, *Circulation* **104**, 3069 (2001).
- [47] R. Morgan, M. A. Colman, H. Chubb, G. Seemann, and O. V. Aslanidi, *Frontiers in physiology* **7**, 474 (2016).
- [48] A. Rudenko and A. Panfilov, *Studia Biophysica* **98**, 183 (1983).
- [49] Z. Qu and J. N. Weiss, *American Journal of Physiology-Heart and Circulatory Physiology* **289**, H1692 (2005).
- [50] O. Berenfeld, *Clinical Medicine Insights: Cardiology* **10**, CMC (2016).
- [51] V. Fast and A. Pertsov, *Biofizika* **35**, 478 (1990).
- [52] J. Jalife and R. Gray, *Acta Physiologica Scandinavica* **157**, 123 (1996).
- [53] C. H. Roney, J. D. Bayer, S. Zahid, M. Meo, P. M. Boyle, N. A. Trayanova, M. Haïssaguerre, R. Dubois, H. Cochet, and E. J. Vigmond, *EP Europace* **18**, iv146 (2016).
- [54] C. Antzelevitch and J. Fish, *Basic research in cardiology* **96**, 517 (2001).
- [55] Z. A. McCrossan, R. Billeter, and E. White, *Cardiovascular research* **63**, 283 (2004).
- [56] F. L. Burton and S. M. Cobbe, *Cardiovascular research* **50**, 10 (2001).
- [57] N. Szentadrassy, T. Banyasz, T. Biro, G. Szabo, B. I. Toth, J. Magyar, J. Lazar, A. Varro, L. Kovacs, and P. P. Nanasi, *Cardiovascular research* **65**, 851 (2005).
- [58] P. C. Viswanathan and Y. Rudy, *Circulation* **101**, 1192 (2000).
- [59] A. Schmidt, C. F. Azevedo, A. Cheng, S. N. Gupta, D. A. Bluemke, T. K. Foo, G. Gerstenblith, R. G. Weiss, E. Marbán, G. F. Tomaselli, et al., *Circulation* **115**, 2006 (2007).
- [60] C. Antzelevitch, *Heterogeneity and cardiac arrhythmias: an overview* (2007).
- [61] A. Mikhailov and V. Krinsky, *Physica D: Nonlinear Phenomena* **9**, 346 (1983).
- [62] A. T. Winfree, *Chaos: An Interdisciplinary Journal of Nonlinear Science* **1**, 303 (1991).
- [63] A. Mikhailov, V. Davydov, and V. Zykov, *Physica D: Nonlinear Phenomena* **70**, 1 (1994).
- [64] V. Hakim and A. Karma, *Physical review E* **60**, 5073 (1999).
- [65] D. Margerit and D. Barkley, *Chaos: An Interdisciplinary Journal of Nonlinear Science* **12**, 636 (2002).
- [66] V. Zykov, *Physica D: Nonlinear Phenomena* **238**, 931 (2009).
- [67] J. Löber and H. Engel, *Chaos: An Interdisciplinary Journal of Nonlinear Science* **23**, 043135 (2013).
- [68] D. Barkley, *Physical Review Letters* **72**, 164 (1994).

- [69] M. Potse, B. Dubé, J. Richer, A. Vinet, and R. M. Gulrajani, *IEEE Transactions on Biomedical Engineering* **53**, 2425 (2006).
- [70] T. Zeng, G. C. Bett, and F. Sachs, *American Journal of Physiology-Heart and Circulatory Physiology* **278**, H548 (2000).
- [71] A. Kamkin, I. Kiseleva, and G. Isenberg, *Cardiovascular research* **48**, 409 (2000).
- [72] S. A. Thompson, C. R. Copeland, D. H. Reich, and L. Tung, *Circulation* **123**, 2083 (2011).
- [73] A. Panfilov, R. Keldermann, and M. Nash, *Proceedings of the National Academy of Sciences* **104**, 7922 (2007).

Supplementary Material: An *in silico* study of electrophysiological parameters that affect the spiral-wave frequency in cardiac tissue

Mahesh Kumar Mulimani,^{1,*} Soling Zimik,^{1,†} and Rahul Pandit^{1,‡}

¹Centre for Condensed Matter Theory, Department of Physics,
Indian Institute of Science, Bangalore 560012, India.

PACS numbers: 87.19.Xx, 87.15.Aa

We give below the following supplementary information, which is mentioned in the main paper:

1. We show in Figs. S1 (a) and (b) the contributions of various ion-channel conductances and ion-pump parameters to the upstroke-velocity (a) $\frac{dV}{dt}_{max}$ and (b) the APD, respectively. We then use parameter-sensitivity analysis, specifically the Principal-Least-Squares regression analysis (PLS), which is described in detail in Ref. [1]. We generate these data by pacing the cell with a pacing-cycle-length PCL= 1s; and we record the last, steady-state AP and $\frac{dV}{dt}_{max}$. B_{pls} , shown on the vertical axes, is the regression coefficient that gives the extent to which the parameter, shown on the horizontal axis, controls (a) $\frac{dV}{dt}_{max}$ and (b) the APD. Positive (negative) value of B_{pls} imply that an increase in the parameter increases (decreases) the value of (a) $\frac{dV}{dt}_{max}$ and (b) the APD. We observe that G_{Na} controls $\frac{dV}{dt}_{max}$ most; this is followed by the $Na - K$ ion-exchanger pump (P_{NaK}); the other conductances and ion-pump parameters do not affect $\frac{dV}{dt}_{max}$ significantly.
2. In Fig. S2 we show spiral-tip trajectories and how the radius r , of the averaged circular trajectory, varies with the different conductances and ion-pump parameters in the TP06 model; the columns are labelled by the values of S_G (Eq.6 in the main paper), which multiply only the conductance or ion-pump parameter that labels a row (all other conductances are held at their control values as we move along a row in Fig. S2).
3. In Figs. S3 (a)-(f) we give plots versus S_G of r , CV, and ω (see the main paper), for various conductances and ion-pump parameters in the TP06 model.
4. In Figs. S4 (a)-(d) we show the dependence of r on the APD, which is tuned by changing the conductances (a) G_{CaL} , (b) G_{Kr} , (c) G_{Ks} and G_{K1} , respectively.
5. In Fig. S5 we show spiral-tip trajectories and how the radius r , of the averaged circular trajectory, varies with S_D , the non-dimensionalised diffusion coefficient (Eq.6 in the main paper); all conductances and ion-pump parameters are held at their control values.
6. In Fig. S6 we show tip trajectories of spiral waves in a tissue with randomly dispersed inexcitable obstacles (**Model I** in the main paper) for four different values of p_o .
7. In Fig. S7 we show the linear fit (black line) to data points from our measurements of ω and $\frac{CV}{2\pi r}$ for all the electrophysiological parameters we use; the diamonds show data points from two of our studies with randomly distributed inexcitable obstacles. The quality of the fit, for the range of values shown is $R^2 = 88.9\%$, if we leave out the points indicated by diamonds.
8. In Table.S1, we show for different electrophysiological parameters the observed frequency of the spiral tip ω_{tip} and the frequency of the spiral wave calculated by using Fourier analysis of the time series data $\omega \equiv \omega_{Fourier}$ (see the main paper). We calculate the ω_{tip} by noting down the time duration where the spiral tip completes

*Electronic address: maheshk@iisc.ac.in ;

†Electronic address: solyzk@gmail.com ;

‡Electronic address: rahul@iisc.ac.in;

also at Jawaharlal Nehru Centre For Advanced Scientific Research, Jakkur, Bangalore, India

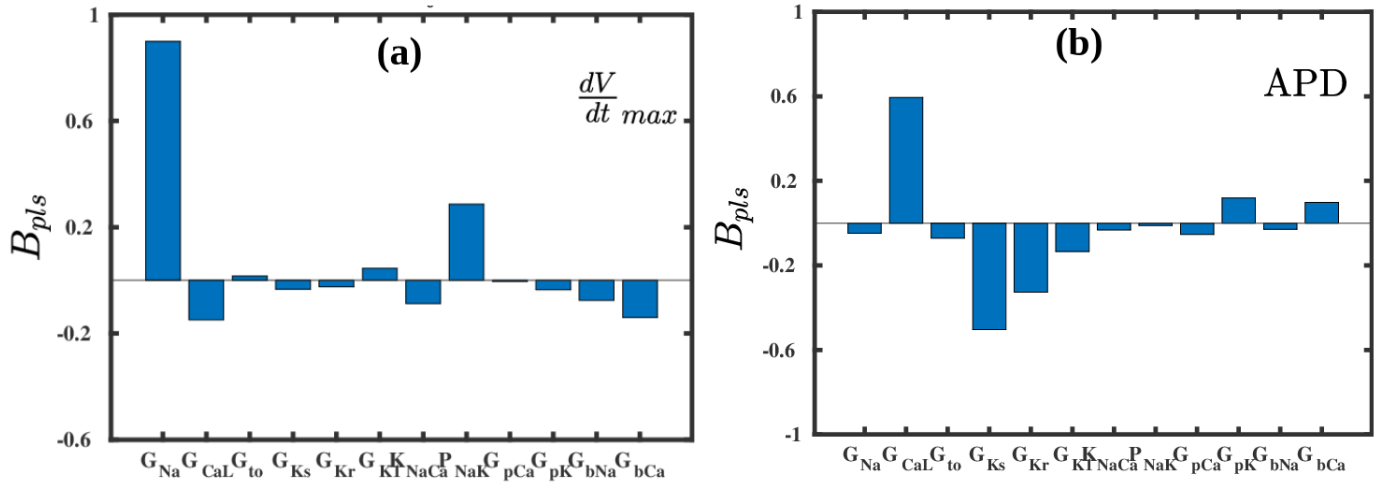


FIG. S1: B_{pls} , shown on the vertical axes, is the regression coefficient that gives the extent to which the parameter, shown on the horizontal axis, controls (a) $\frac{dV}{dt} max$ and (b) the APD. Positive (negative) value of B_{pls} imply that an increase in the parameter increases (decreases) the value of (a) $\frac{dV}{dt} max$ or (b) the APD. For the details of sensitivity analysis see Ref. [1].

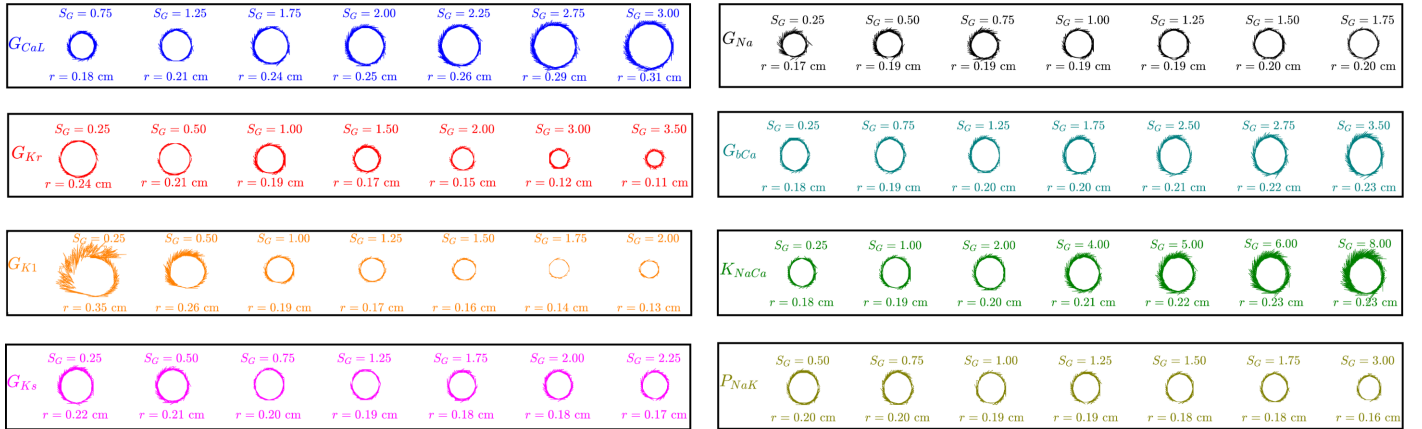


FIG. S2: Spiral-tip trajectories illustrating how the radius r , of the averaged circular trajectory, varies with the different conductances and ion-pump parameters in the TP06 model; the columns are labelled by the values of S_G (Eq.6 in the main paper), which multiply only the conductance or ion-pump parameter that labels a row (all other conductances are held at their control values as we move along a row in Fig. S2); G_{to} , G_{pK} and G_{bNa} , do not affect r , CV, and ω significantly.

one complete rotation.

$$\omega_{tip} = \frac{CV_{tip}}{(2\pi r)} \quad (1)$$

$$CV_{tip} = \frac{2\pi r}{T} \quad (2)$$

$$\omega_{tip} = \frac{1}{T} \quad (3)$$

T is the period of the spiral tip.

- Movie-M1:** A movie from our *in silico* study showing the drift of a spiral wave (via pseudocolor plots of the transmembrane potential V_m) in the presence of gradient in the fibroblast density; the black star in the movie indicates the position of the highest fibroblast density (see text in the main paper).

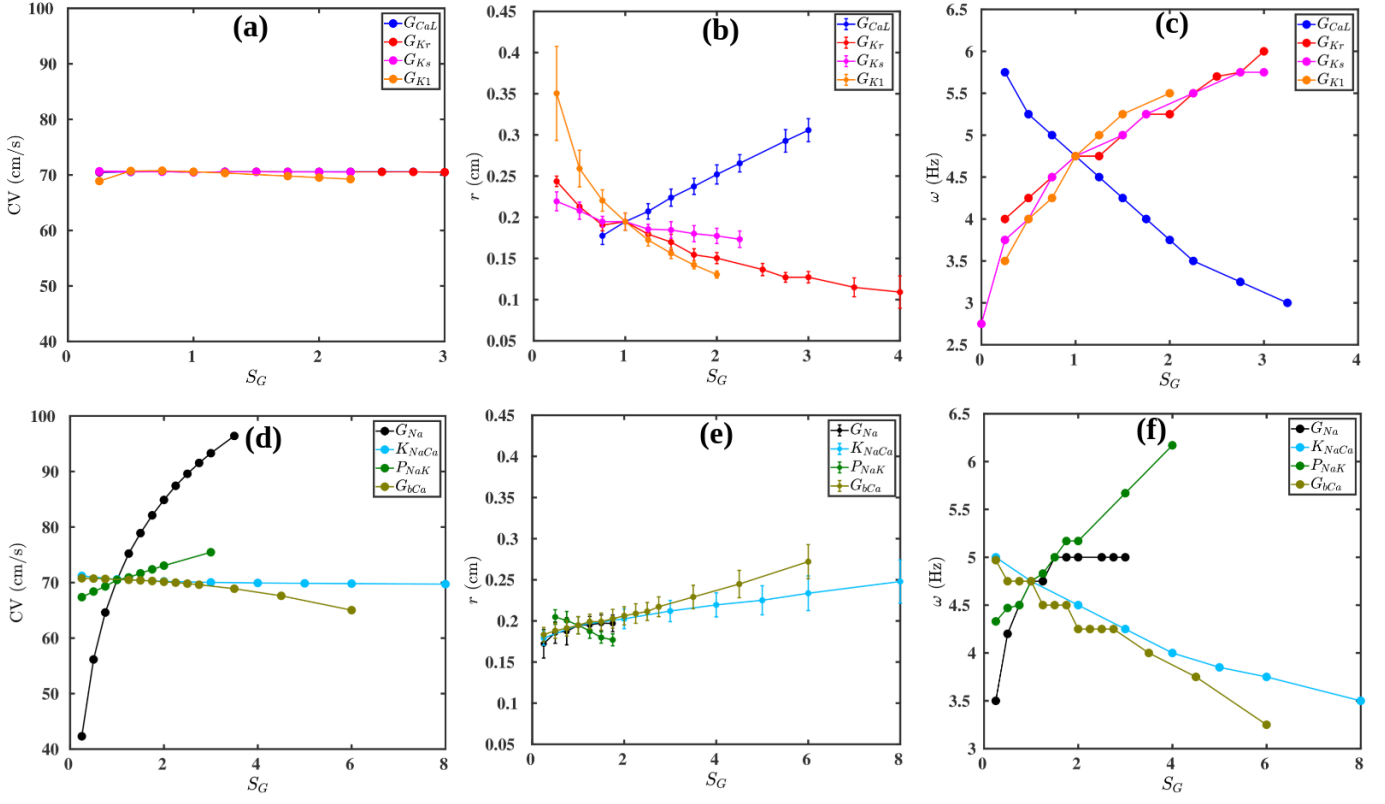


FIG. S3: (a)-(f) Plots versus S_G of r , CV, and ω (see the main paper), for various conductances and ion-pump parameters in the TP06 model.

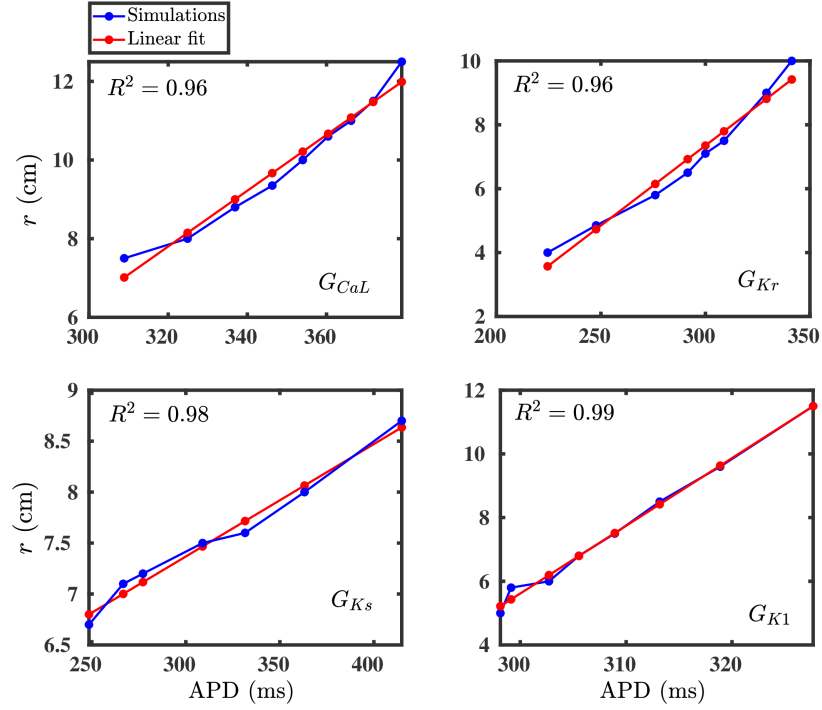


FIG. S4: (a)-(d) Plots showing the dependence of r on the APD, which is tuned by changing the conductances (a) G_{CaL} , (b) G_{Kr} , (c) G_{Ks} and G_{K1} , respectively. R^2 in the plots show the goodness of the fit.

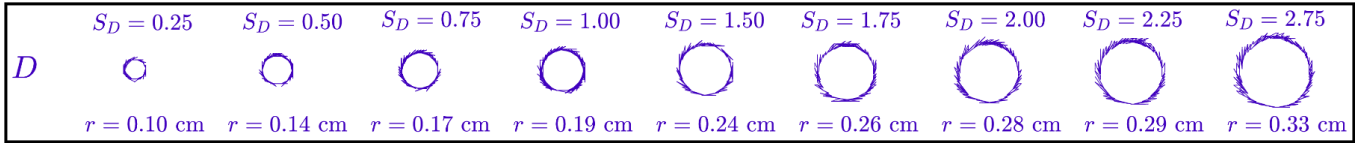
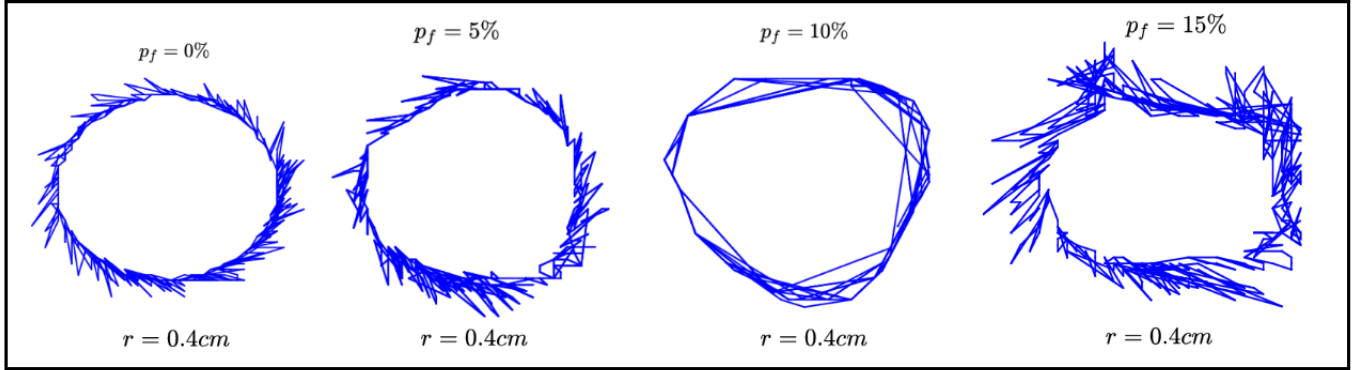


FIG. S5: Spiral-tip trajectories illustrating how the radius r , of the averaged circular trajectory, varies with S_D , the non-dimensionalised diffusion coefficient (Eq.6 in the main paper); all conductances and ion-pump parameters are held at their control values.



(A) Spiral tip trajectories

FIG. S6: Tip trajectories of spiral waves in a tissue with randomly dispersed inexcitable obstacles (**Model I** in the main paper) for four different values of p_o .

References

- [1] M. K. Mulimani, A. R. Nayak, and R. Pandit, Physical Review Research **2**, 033443 (2020).

| Electrophysiological parameter | Time period of spiral tip (T) in (ms) | $\omega_{tip} = \frac{1}{T}$ (Hz) | $\omega_{Fourier}$ (Hz) |
|--------------------------------|---------------------------------------|-----------------------------------|-------------------------|
| $G_{Na_{max}} \times 0.75$ | 220 | 4.54 | 4.5 |
| $G_{CaL_{max}} \times 0.75$ | 200 | 5 | 5 |
| $G_{Kr_{max}} \times 2.75$ | 210 | 5.77 | 5.75 |
| $D \times 2.75$ | 210 | 4.76 | 4.75 |
| $p_f = 5\%$ | 220 | 4.54 | 4.5 |
| $p_f = 10\%$ | 225 | 4.44 | 4.5 |
| $p_f = 15\%$ | 240 | 4.17 | 4.5 |
| $p_f = 30\%$ | 260 | 3.85 | 4.5 |

TABLE S1: The table shows the observed frequency of the spiral tip ω_{tip} (see Eq. 3) and the frequency calculated from the Fourier analysis $\omega_{Fourier}$ (see text) for a few representative electrophysiological parameters.

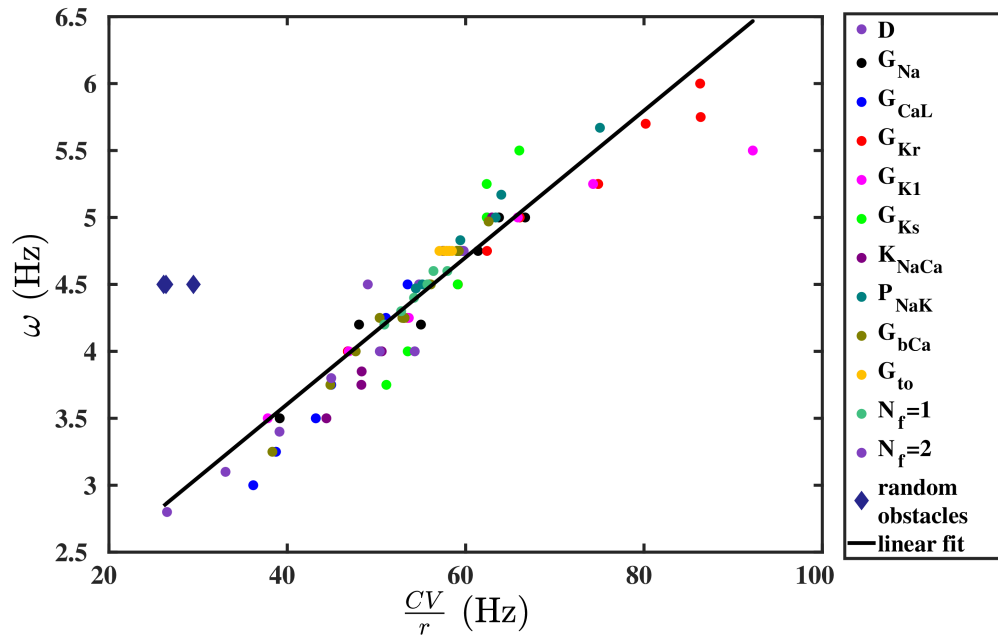


FIG. S7: The linear fit (black line) to data points from our measurements of ω and $\frac{CV}{2\pi r}$ for all the electrophysiological parameters we use; the diamonds show data points from two of our studies with randomly distributed inexcitable obstacles. The quality of the fit, for the range of values shown is $R^2 = 88.9\%$, if we leave out the points indicated by diamonds.